GOES-10 microphysical retrievals in marine warm clouds: Multi-instrument validation and daytime cycle over the southeast Pacific

David Painemal,[1] Patrick Minnis,[1] J. Kirk Ayers,[2] and Larry O'Neill[3]

Received 22 March 2012; revised 27 June 2012; accepted 8 August 2012; published 13 October 2012.

[1] The daytime evolution of warm cloud microphysical properties over the southeast Pacific during October–November 2008 is investigated with optical/infrared retrievals from the Tenth Geostationary Operational Environmental Satellite (GOES-10) imager. GOES-10 retrievals, produced at NASA Langley Research Center, are validated against in situ aircraft observations and with independent satellite observations. Comparisons with in situ observations reveal high linear correlations (r) for cloud effective radius (r_e) and optical thickness (τ) (r = 0.89 and 0.69 respectively); nevertheless, a GOES-10 positive mean r_e bias of 2.3 μm is apparent, and consistent with other previously reported satellite biases. Smaller biases are found for liquid water path (LWP) and an adiabatic-based cloud droplet number concentration (N_d), both variables derived by combining r_e and τ. In addition, GOES-10 observations are well correlated with their Moderate Resolution Imaging Spectroradiometer (MODIS) counterparts, but with smaller biases and root-mean-square errors for the Aqua satellite passes, arguably associated with a better calibrated MODIS-Aqua instrument relative to MODIS-Terra. Furthermore, the excellent agreement between GOES-10 LWP and microwave-based satellite retrievals, especially at high solar zenith angles (>60°), provide further evidence of the utility of using GOES-10 retrievals to represent the daytime cloud cycle. In terms of the daytime cycle, GOES-10 observations show an afternoon minimum in LWP and an increase thereafter, consistent with satellite microwave climatologies. The τ cycle explains most of the LWP variance with both variables in phase, minima near noon along the coast, and a 13:30–14:00 local solar time (LST) minimum offshore. In contrast, r_e is not exactly in phase with LWP and τ, having a minimum approximately at 12:30 LST throughout the domain. A unique feature is a striking r_e maximum along the coast at 16:15 LST, concomitant with a faster τ recovery. An explanation for a coastal r_e afternoon maximum is lacking although this is consistent with an enhancement of the updraft velocity reported in previous modeling studies. Finally, the GOES-derived N_d ($N_d \propto \tau^{1/2} r_e^{-5/2}$) shows a complex daytime cycle with maxima at 7:15 and 13:15 LST. While the first maximum is driven by large τ, the second one is mainly explained by a minimum in r_e.

Citation: Painemal, D., P. Minnis, J. K. Ayers, and L. O'Neill (2012), GOES-10 microphysical retrievals in marine warm clouds: Multi-instrument validation and daytime cycle over the southeast Pacific, *J. Geophys. Res.*, *117*, D19212, doi:10.1029/2012JD017822.

1. Introduction

[2] Marine stratocumulus clouds have been largely acknowledged as a key component of the climate system [e.g., *Klein and Hartmann*, 1993]; and their insufficient representation in numerical models is a main source of spread among models, particularly in eastern boundary current regions [*Bony and Dufresne*, 2005]. Improvements in numerical models require an accurate description of the marine warm cloud variability at different time scales. The investigation of the diurnal cycle in the cloud properties has received less attention from a satellite perspective. Although the diurnal cycle in cloud cover has been relatively well documented [e.g., *Minnis and Harrison*, 1984; *Rozendaal et al.*, 1995; *Zuidema et al.*, 2009], a complete description of the cloud radiative properties can only be achieved with observations of cloud microphysics. This will improve understanding of the regional-scale link between cloud microphysics and boundary layer processes such as entrainment, subsidence,

[1]NASA Langley Research Center, Hampton, Virginia, USA.
[2]Sciences System and Applications Inc., Hampton, Virginia, USA.
[3]College of Earth, Ocean, and Atmospheric Sciences, Oregon State University, Corvallis, Oregon, USA.

Corresponding author: D. Painemal, NASA Langley Research Center, Hampton, VA 23681, USA. (david.painemal@nasa.gov)

0148-0227/12/2012JD017822

and boundary layer depth evolution; and therefore, allow a better description of the atmospheric factors that drive the variability in cloud properties. In addition, the accurate assessment of the daytime cycle in cloud microphysics is valuable for testing the representativeness of numerical models [e.g., *Hannay et al.*, 2009] and for calculating or measuring the radiation budget at the surface and the top of the atmosphere [*Young et al.*, 1998].

[3] Previous studies mainly rely on multiple satellite microwave observations to derive the diurnal cycle in vertically integrated water content, or liquid water path (*LWP*) [e.g., *Zuidema and Hartmann*, 1995; *Wood et al.*, 2002; *O'Dell et al.*, 2008]. These *LWP* data sets reveal a dominant diurnal cycle with the largest amplitudes observed over the southern hemisphere marine stratocumulus regimes. In general terms, the daytime cycle shows an early morning maximum and an afternoon minimum linked to solar radiative heating. Interestingly, unlike most of the low cloud regimes, a unique semidiurnal cycle is evident along the west coast of South America, possibly modulated by a southwestward propagating subsidence wave triggered by the Andes cordillera solar heating [*Garreaud and Muñoz*, 2004; *Wood et al.*, 2009]. The relatively well documented LWP diurnal cycle contrasts with the largely unknown diurnal -and daytime- evolution of cloud optical thickness (τ) and effective radius (r_e). Investigations of diurnal changes of r_e and τ are hampered by a lack of operational satellite-based cloud retrievals with an adequate temporal resolution. Even though this is resolved by instruments onboard geostationary platforms such as the Geostationary Operational Environmental Satellite (GOES), the lack of retrieval validation make it difficult to determine whether the observed diurnal cycle is a physical representation or is the mere consequence of algorithm/instrument artifacts. Despite these difficulties, a few investigations have studied the r_e and τ diurnal cycle with satellite visible and infrared observations [e.g., *Minnis et al.*, 1992; *Greenwald and Christopher*, 1999; *Oku et al.*, 2010]. These analyses show overall larger r_e during the early morning, in connection with large LWP, and an afternoon cloud optical thinning consistent with solar radiative heating. Nevertheless, the processes controlling the daytime variability might include other factors in addition to the solar heating. In fact, the influence of advected continental aerosol adds further complexity [*Sandu et al.*, 2008], and might eventually trigger different feedbacks between the cloud deck and other processes such as precipitation or entrainment [e.g., *Ackerman et al.*, 2004].

[4] In this paper, we document the daytime cycle in cloud microphysics (r_e, τ, and cloud droplet number concentration) derived from GOES-10 imager radiances over the southeast Pacific, during the October–November 2008 time period. Furthermore, we tackle the task of assessing the accuracy of the GOES-10 cloud retrievals by carrying out a multi-instrument comparison with independent microwave and visible/near infrared satellite data sets. A focus on the southeast Pacific domain is justified by its climate and radiative significance, with unique modes of variability [e.g., *O'Neill et al.*, 2011], and high albedo susceptibility to changes in cloud microphysics [e.g., *Painemal and Minnis*, 2012]. Moreover, the period of study allows us to take advantage of in situ aircraft observations of cloud microphysics during the VAMOS Ocean-Cloud-Atmosphere-Land System Regional Experiment (VOCALS-Rex) [*Wood et al.*, 2011].

2. Data Set

[5] We primarily rely on cloud retrievals derived from GOES-10 imager radiances that were analyzed at NASA Langley Research Center. The GOES-10 visible channel was calibrated against the Aqua MODIS channel-1 radiances following the approach of *Minnis et al.* [2002]. Cloud optical thickness and droplet effective radius were derived at a ~4-km spatial resolution, using the algorithms described in *Minnis et al.* [2008a, 2011] and processed as reported by *Minnis et al.* [2008b]. The 4-km resolution is native for the GOES infrared channels, but the visible channel resolution is 1-km. The 1-km data were sampled every fourth scan line and element to achieve a 4-km resolution. In this algorithm, the GOES-10 r_e and τ are primarily functions of the 3.9 and 0.65 μm radiances, respectively. The period of study encompasses October and November 2008, with the retrievals produced at 30-min intervals (typically at X:15 and X:45 UTC). Unless otherwise stated, the cloud observations are averaged to a 0.25° resolution. The GOES-10 cloud fraction is calculated as the ratio of pixels with successful cloud retrievals to the total number of pixels in a 0.25° × 0.25° area. While the GOES-based cloud properties are computed for solar zenith angles (SZA) less than 83°, we limit the analysis to observations having SZA < 70°, or local solar time (LST) approximately between 7 and 16 LST. The viewing zenith angle (VZA) over the study region encompasses values between 22 and 40°; and therefore, is less susceptible to cloud fraction dependence on VZA [*Minnis*, 1989]. We limit this investigation to 0.25° regions having warm clouds with GOES-10 cloud top temperatures greater than 0°C, $\tau > 1$, and cloud cover exceeding 90% (cloud fraction of 0.9).

[6] Liquid water path (LWP) and cloud droplet number concentration (N_d) are calculated assuming an adiabatic-like vertical stratification [*Painemal and Zuidema*, 2011 and references therein] and applied to all the visible/near-infrared data sets used in this study:

$$LWP = \rho_w \frac{5}{9} r_e \cdot \tau \tag{1}$$

$$N_d = 1.4067 \cdot 10^{-6} \left[\mathrm{cm}^{-1/2}\right] \cdot \frac{\tau^{1/2}}{r_e^{5/2}} \tag{2}$$

[7] This definition of LWP is used in lieu of and is 17% less than the LWP values provided by the GOES-10 products. The latter is based on the assumption that r_e derived with the 3.9-μm channel represents the entire cloud column. For stratus and stratocumulus decks, the adiabatic assumption provides a more accurate estimate of LWP [*Bennartz*, 2007].

[8] Observations collected during VOCALS-REx are used to assess the accuracy of the GOES-10 cloud property retrievals. This analysis follows the methodology described in *Painemal and Zuidema* [2011] (hereafter PZ11), but applied to GOES-10 observations. A total of 41 vertical cloud microphysical profiles collected by a C-130 aircraft were collocated with GOES-10 pixels, and are used to

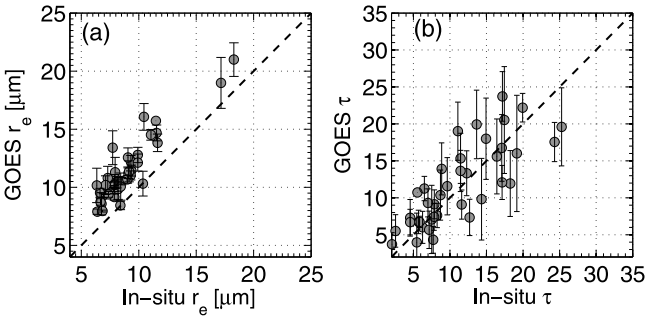

Figure 1. Scatterplot between GOES and in situ observations: (a) cloud optical thickness and (b) cloud effective radius. Vertical error bars denote the 20 km GOES standard deviation.

compute r_e at the cloud top, LWP, τ, and a vertically averaged N_d.

[9] The retrievals of GOES-10 cloud microphysics are also assessed by comparison with the standard visible/near-infrared level-2 Collection-5 retrievals from the Moderate Resolution Imaging Spectroradiometer (MODIS) produced by the MODIS Atmosphere team at a 1-km resolution (*Platnick et al.* [2003], Level 2 Cloud Product, available at http://ladsweb.nascom.nasa.gov/). We use τ and r_e derived from the MODIS 0.65 and 3.8-μm radiances. The comparison is limited to MODIS granules collocated within 20 min of the GOES-10 scan at 10:45 LST (Terra satellite) and 13:45 LST (Aqua satellite). In addition to the MODIS team retrievals, cloud microphysical properties were independently derived from MODIS Terra and Aqua radiances for the Clouds and the Earth's Radiant Energy System (CERES), Single Scanner Footprint Edition 2 (SSF, available at http://eosweb.larc.nasa.gov/), using algorithms nearly identical to those applied to GOES-10 data [*Minnis et al.*, 2011, 2012]. The CERES SSF cloud retrievals are available at the CERES footprint resolution (~20 km) as averages computed from subsampled 1-km cloud microphysical retrievals using convolution with the CERES scanner point spread function. The CERES cloud processing uses every fourth 1-km pixel from every other scan line [*Minnis et al.*, 2011]. The CERES results are also used to evaluate consistency with the GOES-10 retrievals.

[10] Since the GOES-MODIS comparisons are limited to low SZAs, we complement the analysis with liquid water paths retrieved from four satellite-based microwave instruments: the Tropical Rainfall Measuring Mission (TRMM) Microwave Imager (TMI); the Special Sensor Microwave Imager (SSM/I) on the Defense Meteorological Satellite Program (DMSP) F13 and F15 satellites; and the Advanced Microwave Scanning Radiometer on the Earth Observing System (EOS)-Aqua (AMSR-E) satellite. The LWP values were retrieved and provided by Remote Sensing Systems (RSS, http://www.ssmi.com/) and determined for each satellite at a 0.25° resolution using the methods described by *Wentz* [1997], *Wentz and Meissner* [2000], and *Hilburn and Wentz* [2008]. In particular, SSM/I and TMI retrievals at SZAs near 60°–70° allow the testing of GOES-10 observations under conditions with potential enhancement of 3D radiative transfer effects in the retrievals. The RSS LWP products correspond to version 4 for TMI and version 6 for AMSR-E and the SSM/I F13 and F15.

3. Multi-instrument Comparisons

3.1. GOES-10 and Aircraft Observations During VOCALS-REx

[11] The individual GOES-10 pixel retrievals were averaged to a 20-km resolution and compared against collocated C-130 aircraft in situ data within 18 min of the vertical profile occurrence. The pixel location was first corrected by the distance traveled by the cloud during the elapsed time between the satellite pass and the vertical profile occurrence, assuming a mean advective velocity given by the mean wind speed of each aircraft profile (PZ11). Because of their low altitudes and small VZAs, parallax corrections were unnecessary.

[12] The in situ cloud properties were derived from the combined cloud and precipitation (drizzle) mode droplet spectra measured by a Cloud Droplet Probe (CDP) and Particle Measuring System's Two-Dimensional Cloud optical array probe (2D-C) respectively. The in situ cloud top r_e was calculated by averaging the four measurements closest to the cloud top. The profiles' liquid water content and volume extinction coefficient (estimated from the second moment of the droplet spectra) were vertically integrated to produce LWP and τ respectively.

[13] The clouds sampled by the C-130 aircraft typically had an adiabatic-like vertical structure, that is, the liquid water content and r_e increase monotonically with height (see Figure 5 in PZ11). Although some profiles showed evidence of cloud top mixing with the clear air above (i.e., water content decreased near the cloud top), r_e is a maximum at the cloud top, except for a few profiles that had significant precipitation (drizzle mode water path larger than 20 g m^{-2}). Profiles of N_d were mostly constant with height, consistent with r_e and water content profiles (PZ11).

[14] The GOES-10 r_e values show a high correlation with observations (Figure 1a, r = 0.91), although the GOES-10 r_e is systematically larger, with a mean bias of 2.4 μm (22%), and a root-mean-square error (RMSE) of 1.15 μm. No evidence of SZA-dependent differences between the satellite-derived and in situ r_e was found (not shown). The GOES-10 r_e positive bias is also qualitatively confirmed by an independent study during VOCALS-Rex over 20°S and 72°W [*Zheng et al.*, 2011]. The positive bias of the GOES-10 r_e found here is surprisingly similar to the one found between MODIS and the same in situ data set by PZ11 (2.08 μm). An explanation for this bias is still lacking, although it might include factors related to the thermal emission, water vapor absorption, and 3D radiative effects, among others. PZ11 showed that this bias is unlikely to be associated with the vertical structure of r_e, water content, or drizzle occurrence. In terms of τ, GOES-10 shows good agreement with the in situ observations (Figure 1b), with a correlation of 0.79, a RMSE of 3.7, and a mean bias of 0.54 (6%), a value likely within the uncertainty range of the in situ τ (PZ11).

[15] The GOES-10 LWP is linearly correlated with the in situ measurements at a level of 0.84, and has a positive bias of 9.9 g m^{-2} (14.7%), attributed to the GOES-10 r_e overestimate, and a RMSE of 26.9 g m^{-2} (Figure 2a). In addition, the GOES-based N_d agree well with the aircraft

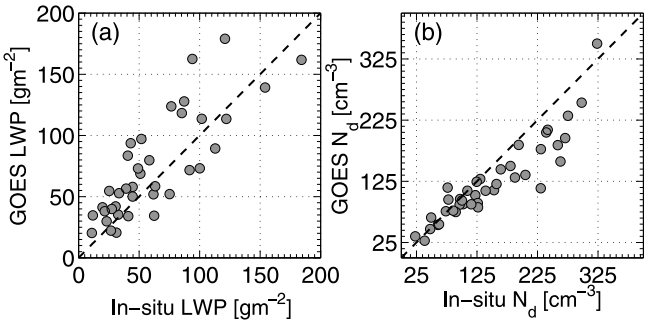

Figure 2. Scatterplot between GOES and in situ observations: (a) liquid water path and (b) N_d.

observations, yielding a high correlation (r = 0.91) and a negative bias (−24.3 cm^{-3}, −20%) and a RMSE of 36 cm^{-3} (Figure 2b). The good agreement for N_d, also found for MODIS observations, was attributed to an appropriate selection of constant parameters in equation (2), which are able to counteract the effect of an overestimate in r_e (PZ11).

3.2. GOES-10 and MODIS Cloud Microphysics

[16] A more systematic assessment of the GOES-10 r_e and τ retrievals is attained by comparing GOES-10 observations with other satellite data sets. We first compare GOES-10 against MODIS Atmosphere Team retrievals [*Platnick et al.* 2003], with all the observations re-gridded to a 0.25° resolution. An analysis of the re-gridded pixels is then carried out between the GOES-10 images and Terra-MODIS and Aqua-MODIS granules collocated within 20 min of the GOES-10 scan at 10:45 and 13:45 LST, respectively. Similar to the GOES analysis, the MODIS cloud fraction is calculated as the ratio of pixels with successful cloud retrievals to the total number of pixels in a 0.25° × 0.25° area. In addition, we limit the analysis to 0.25° grids with cloud fraction greater than 90%, τ larger than 1, and cloud top temperatures greater than 0°C.

[17] The GOES-10 and MODIS Atmosphere Team cloud variables (Figures 3 and 4) are in excellent agreement, with correlations exceeding 0.88 (Tables 1a and 1b), although some differences between Terra and Aqua are apparent. The GOES-10 and Terra matches show the largest disagreement, with greater mean bias and root-mean-square (RMS) difference relative to (Aqua-MODIS)-GOES, and a MODIS negative offset (mean bias −1.15 μm, 9.9%) that increases with r_e, with a noticeable deviation from the 1:1 line for radii larger than 10 μm, with a GOES-(Terra-MODIS) slope of 0.77 for radii between 10 and 20 μm (Figure 3a). In contrast, the mean bias for Aqua-GOES is smaller (−0.43 μm), with a better overall agreement (Figure 3c, GOES-Aqua-MODIS slope of 0.91 for radii between 10 and 20 μm). Although further investigation, beyond the scope of this study, may be required to fully elucidate platform differences, the r_e-dependent difference between Terra and GOES-10 likely reflects calibration issues in the Terra 3.8-μm channel. *Minnis et al.* [2008a] demonstrated that the Terra 3.8-μm brightness temperature is 0.55 K warmer than the Aqua counterpart, causing an ∼0.7 μm reduction in Terra MODIS r_e relative to Aqua [*Minnis et al.*, 2012]. This constant brightness temperature difference does not produce a constant bias in r_e, rather the r_e difference increases with increasing r_e because of the nonlinear relationship between r_e

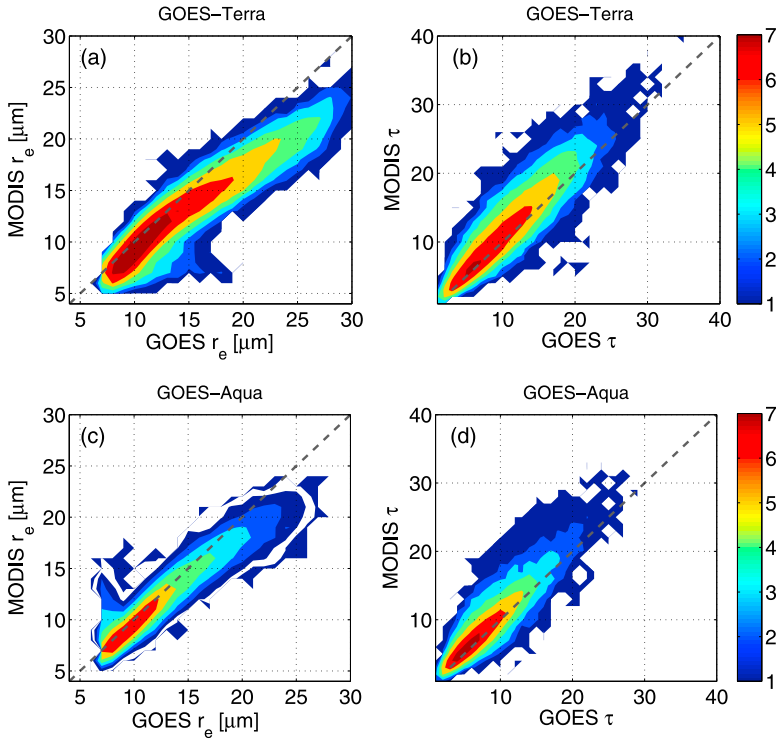

Figure 3. Comparison of GOES and MODIS team observations. The colors indicate the number of samples per bin (natural logarithm scale). (a) GOES and MODIS-Terra r_e, (b) GOES and MODIS-Terra τ, (c) GOES and MODIS-Aqua r_e, and (d) GOES and MODIS-Aqua τ.

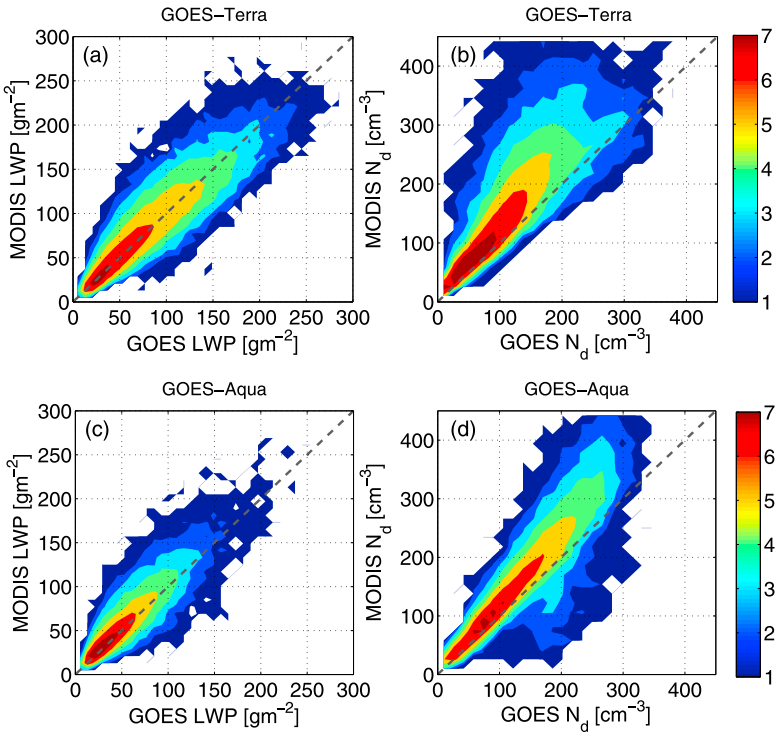

Figure 4. Comparison of GOES and MODIS team observations. The colors indicate the number of samples per bin. (a) GOES and MODIS-Terra LWP, (b) GOES and MODIS-Terra N_d, (c) GOES and MODIS-Aqua LWP, and (d) GOES and MODIS-Aqua N_d.

and the reflected component of the 3.8-μm radiance. Thus, the behavior of the GOES-10 r_e relative to its Terra and Aqua MODIS counterparts in Figure 3 is consistent with MODIS 3.8-μm calibration differences.

[18] In terms of τ, both Terra and Aqua MODIS are larger than GOES, with a mean bias of 1.2 (10.5%) and 0.9 (10.2%) respectively. The MODIS τ positive bias may be connected, at some level, to the MODIS Team's process of discarding pixels near cloud edges or optically thin pixels and, therefore, yielding larger τ values than GOES-10 [*Minnis et al.*, 2012]. This is likely to be a minor effect here since only regions having CF > 90% are used. The coarser GOES-10 spatial resolution may also account for the lower GOES-10 τ due to clear-sky contamination or to the nonlinear relationship between τ and reflected radiance. The latter is likely to come into play when there is significant sub-pixel scale variability within each GOES 4-km pixel. The Terra-Aqua τ discrepancies are discussed further below.

Table 1a. Linear Correlation Coefficient, Mean MODIS-Terra and GOES Bias, and Root-Mean-Square Error for r_e, τ, LWP, and N_d[a]

	Correlation Coefficient	Mean Bias (MODIS-GOES)	RMS Differences
r_e	0.94	−1.15 [μm]/(−9.9%)	1.2 [μm]
τ	0.91	1.2/(10.5%)	2.1
LWP	0.91	2.5 [gm^{-2}]/(3.1%)	19.1 [gm^{-2}]
N_d	0.88	33.4 [cm^{-3}]/(25.2%)	39.9 [cm^{-3}]

[a]MODIS retrievals were produced by MODIS Atmosphere team. Total number of samples is 41,146.

[19] The GOES and MODIS secondarily derived variables, namely LWP and N_d, also are highly correlated, with biases explained by offsets in τ and r_e (Figure 4). Interestingly, the competing effect between larger GOES r_e and smaller GOES τ relative to MODIS, yields a bias reduction in LWP, with a mean offset smaller than 4.7 g m^{-2} (Figures 4a and 4c). In terms of N_d (Figures 4b and 4d), the dominant effect of r_e in equation (2) is apparent, producing a larger disagreement (as expected) for Terra and with the offset increasing with N_d (Figure 4b). The main statistics are summarized in Tables 1a and 1b.

[20] An additional consistency test was performed using MODIS retrievals derived by the CERES team (hereafter CERES), produced with a similar algorithm used for the GOES-10 analyses. In order to produce regular grid maps, the retrievals were averaged to 0.5° resolution, because the CERES Single Scanner Footprint product used in the analysis is collocated with the CERES 20-km footprint, and therefore irregularly sampled. Comparisons of the GOES-10 and CERES cloud microphysics (Figure 5) are fairly consistent with those found for the GOES-10 and MODIS team observations: an overall larger bias and RMSE for Terra r_e,

Table 1b. As in Table 1a but for MODIS-Aqua[a]

	Correlation Coefficient	Mean Bias (MODIS-GOES)	RMS Differences
r_e	0.95	−0.43 [μm]/(−4.1%)	0.82 [μm]
τ	0.90	0.9/(10.2%)	1.8
LWP	0.89	4.7 [gm^{-2}]/(8.3%)	14.8 [gm^{-2}]
N_d	0.94	26.2 [cm^{-3}]/(17.9%)	32.6 [cm^{-3}]

[a]Total number of samples is 25,799.

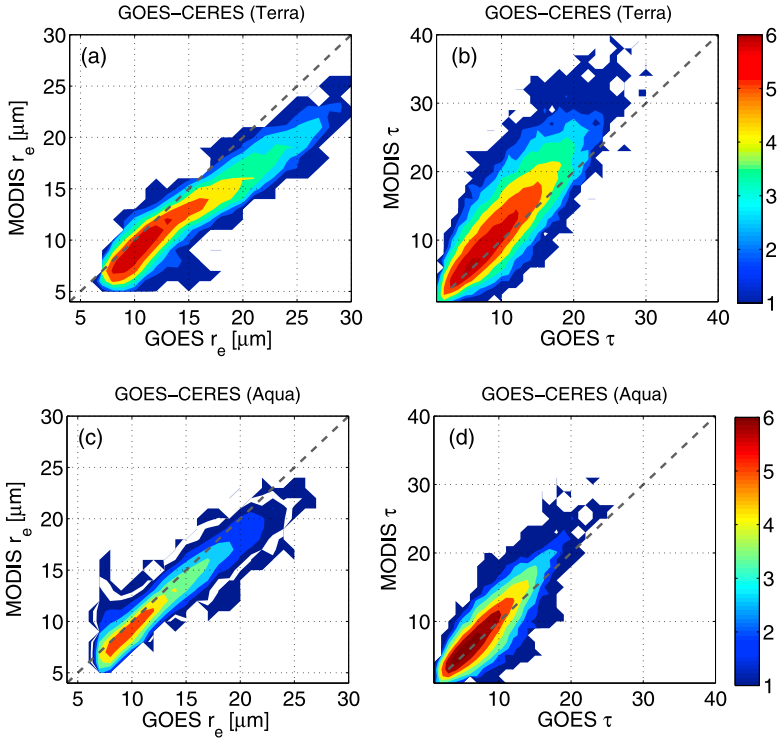

Figure 5. As in Figure 4 but for CERES team retrievals of MODIS r_e and τ, with pixels re-gridded to 0.5° resolution.

with a Terra-CERES underestimate that increases with r_e, and a (Terra-CERES)-GOES τ positive bias in agreement with the MODIS-team-GOES bias (Table 2). It is striking that poorer Terra-CERES agreement with GOES-10 remains regardless of the algorithms used (MODIS or CERES teams), reinforcing the idea of a bias attributed to the Terra 3.8-μm channel calibration. The impact of the resolution differences on the 3.8-μm r_e retrieval differences due to inhomogeneities in the clouds is likely very small, but possibly sufficient to account for discrepancies smaller than 1 μm [e.g., *Zhang and Platnick*, 2011].

[21] General differences between the GOES-10 and CERES τ values cannot be explained by differences in resolution [e.g., *Cahalan et al.*, 1994] because the GOES optical depths were derived using 1-km visible-channel data. Other effects that influence the τ retrievals include r_e and calibration differences, atmospheric absorption by water vapor and ozone, and potential angle-dependencies due to cloud structure. The visible radiances from Terra are smaller relative to Aqua [*Minnis et al.*, 2008c]. Thus, the calibration differences should cause Terra-Aqua differences of the opposite sign. The smaller Terra r_e values have only a relatively minor impact on τ, insufficient to account for τ differences of ~1.2 between the Terra and Aqua retrievals. The CERES and MODIS retrievals both use ozone and water vapor profiles from numerical weather prediction model analyses; the concentrations vary according to the time step of the models. The GOES-10 analysis assumes a monthly variable climatological atmospheric ozone optical depth and a numerical weather prediction model forecast for water vapor. Thus, differences in ozone absorption could impact the results, but they should be the same for each satellite. Yet, a closer examination of the data indicate that, even for GOES-10 τ values exceeding 5, the mean Terra-GOES-10 τ differences are all greater than their Aqua counterparts. Therefore, the use of different ozone concentrations cannot account for the morning-afternoon differences. Changes in cloud structure may be a source of the differences since thinner and fewer clouds are observed by Aqua, but this type of effect should be minimized to some degree by using CF > 90% for the comparisons. Determining the ultimate source of the morning-afternoon MODIS-versus-GOES-10 difference discrepancy remains a topic for future research.

3.3. GOES-10 and Microwave-Base Liquid Water Path

[22] The multisensor assessment of GOES-10 cloud microphysics is further complemented with satellite microwave observations of liquid water path from SSM/I F13 and F15, TMI, and AMSR-E. The microwave LWP values with 0.25° resolution are collocated within 20 min of the GOES-10 images at 6:45, 13:45, and 16:15 LST. SSM/I and TMI

Table 2. Linear Correlation Coefficient, Mean Bias, and RMS Differences Between CERES and GOES[a]

	Correlation Coefficient	Bias (CERES-GOES)	RMS Differences
r_e	0.94/**0.94**	−1.82(−16.4%) **−0.78(6.9%)** [μm]	1.57/**1.2** [μm]
τ	0.87 **0.88**	1.8(19.6%) **0.57(9.6%)**	2.8 **1.8**

[a]Regular and boldface numbers represent the analysis for Terra and Aqua, respectively. Total number of samples is 12,138 for Terra and 8251 for Aqua.

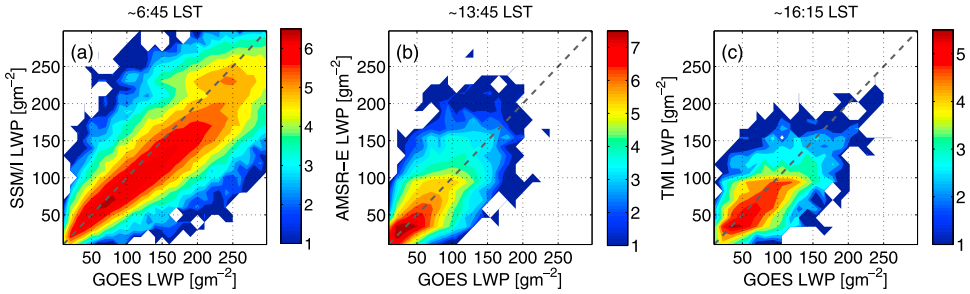

Figure 6. Comparison of GOES and satellite microwave LWP retrievals: (a) GOES versus SSM/I, (b) GOES versus AMSR-E, and (c) GOES versus TMI. SSMI/I, AMSR-E, and TMI, are collocated within 15 min of GOES scan at 8:45, 13:45, and 16:15 LST.

are particularly valuable for testing GOES-10 observations collected in low sun conditions, typically for SZAs between 60° and 70°. The comparison is carried out for overcast cloudy scenes only (determined by GOES), in order to reduce the microwave biases observed in broken clouds [*Horváth and Gentemann*, 2007].

[23] The SSM/I and GOES-10 LWPs at 6:45 LST (Figure 6a) show a strong linear correlation (r = 0.82), with a mean bias of 12.5 g m^{-2} (10.2%) with larger GOES-10 LWPs. The offset increases for LWP greater than 100 g m^{-2}. This trend may be associated with three dimensional radiative transfer effects in the visible/infrared retrievals, which can become more conspicuous in spatially heterogeneous clouds, especially well offshore where LWP is large. However, some of the bias for larger LWP values may also be attributed to the use of a universal rain algorithm applied to values of LWP > 180 g m^{-2} [*Seethala and Horváth*, 2010]. The AMSR-E and GOES-10 LWP retrievals at 13:45 LST (Figure 6b) also correlate well (r = 0.77), with a negligible bias. This result is consistent with other comparisons between MODIS and AMSR-E that showed the smallest bias over marine stratocumulus regimes [e.g., *Borg and Bennartz*, 2007; *Seethala and Horváth*, 2010]. Finally, the TMI and GOES-10 joint histogram (Figure 6c) shows more scatter, with a lower correlation (r = 0.6) but with a small bias (6.2 g m^{-2}, 8.9%, Table 3). Figure 6 also reflects the daytime evolution in LWP, with high values during the morning and a reduction in the afternoon, followed by an LWP recovery, as documented by *O'Dell et al.* [2008].

[24] The agreement between GOES-10 and the different observational platforms reported in this section provide sufficient evidence of the accuracy of the GOES-10 retrievals for representing cloud microphysical properties and resolving daytime variations over the region of study. In the following section, we describe the main features of the stratocumulus daytime cycle and its radiative implications.

4. Daytime Cycle

4.1. General Features

[25] The daytime cycle analysis is based on averaging the GOES-10 LWP, τ, r_e, and N_d values taken at the same local time over the entire study period, yielding 20 mean values between 6:45–16:15 LST.

[26] Zonal samples taken along 21°S at 72°, 76°, and 80°W for cloud fraction (CF) LWP, τ, and r_e are depicted in Figure 7 (black, red, and blue lines, respectively). The samples show a general morning decrease until 12–14 LST and an increase thereafter. In contrast, the CF minima are observed after 14 LST, consistent with an in situ study at 26°S and 80°W [*Painemal et al.*, 2010]. Figure 7 also suggests two different cycles for LWP, with minima near noon for 72°S and 14 LST for 76°–80°W (Figure 7b). The minimum τ is concomitant with the minimum LWP, and is likely its cause since 98% of the LWP variance is explained by τ in this region (Figure 7c). In terms of r_e, smaller mean values near the coast and a westward increase (Figure 7d) are the most significant features. This gradient, previously observed in other satellite data sets and in situ observations, is mainly driven by continental aerosols transported into the cloud deck, especially near the coast [e.g., *Painemal and Zuidema*, 2010]. Unlike τ and LWP, the three zonal points have a rather similar minimum r_e occurrence at around 13 LST, suggesting different diurnal cycle modulations in τ (LWP) and r_e. Moreover, Figure 7c shows two r_e maxima near 8:15 LST and 16:15 LST. Interestingly, the region closest to the continent shows a sharp r_e rise (Figure 7d, black line) starting at 15:15 LST, a trait that will be further investigated in the following sections.

[27] Westward changes in LWP τ, depicted in Figure 7, seem to be in agreement with other observational and modeling evidence [*O'Dell et al.*, 2008; *Wood et al.*, 2009] that show the presence of a characteristic semidiurnal cycle in LWP over the southeast Pacific, along the coast at 15°–25°S, with a dominant diurnal cycle component well offshore [*O'Dell et al.*, 2008; *Wang et al.*, 2011]. Although it is not possible to resolve either the semidiurnal or the diurnal cycle with our observations, we can assess to some extent the relative dominance of the 12 and the 24-h periods by fitting a

Table 3. Microwave-GOES LWP Linear Correlation Coefficient, Mean LWP Microwave-GOES Bias, and RMSE[a]

	Correlation Coefficient	Mean Bias (μwave-GOES)	RMS Differences	Number of Pixels
SSM/I	0.82	−12.5 [gm^{-2}]/−10.2%	35.21 [gm^{-2}]	65341
AMSR-E	0.77	−1.04 [gm^{-2}]/−2.1%	20.65 [gm^{-2}]	29410
TMI	0.66	−6.2 [gm^{-2}]/−8.9%	30.03 [gm^{-2}]	5887

[a]SSMI/I, AMSR-E, and TMI, are collocated within 20 min of GOES scan at 8:45, 13:45, and 16:15 LST. The statistics are calculated for LWP lower than 250 g m^{-2}.

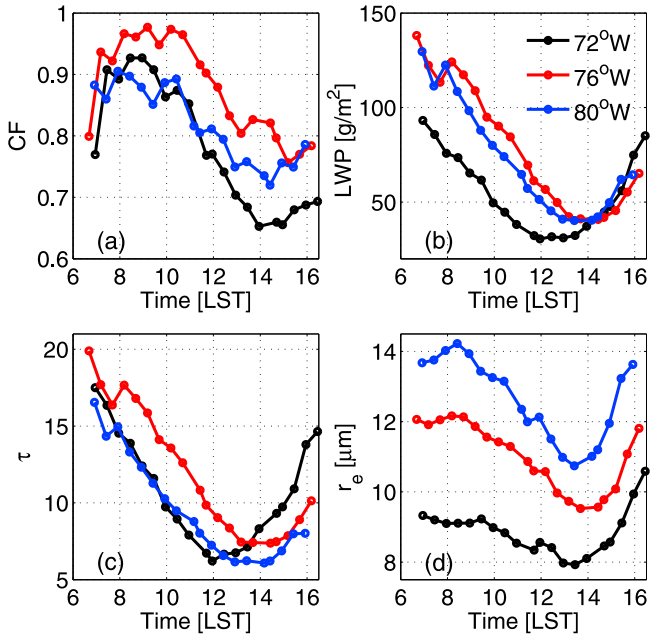

Figure 7. Example of daytime variations in cloud microphysics along 21°S latitude at 72° (black), 76° (red), and 80°W (blue) longitude. (a) CF, (b) LWP, (c) τ, and (d) r_e.

cosine function to our observations. Here, we adopt the use of a simple cosine function:

$$LWP_{fit}(t) = A\cos\left(\frac{2\pi}{T}(t-\phi)\right) + \overline{LWP}. \quad (3)$$

[28] A is the cosine amplitude, T the period, ϕ the phase, and $\overline{LWP}$ the mean daily LWP. $\overline{LWP}$ is the daily mean microwave LWP, during the period of study obtained from the *O'Neill et al.* [2011] climatology. Values for A and ϕ are calculated for 12 and 24-h periods separately using a standard least squares regression. While a more rigorous approach would simultaneously fit both the 12 and 24-h cosines, four unknowns in the regression process would make the calculation less reliable, especially because the observations only partially cover the daily cycle. Instead, we fit individual cosines for the two periods, and then determine which cosine fit has the least RMSE relative to the 30-min composited GOES-10 LWP. The goal here is not to exactly resolve the LWP diurnal variability, but to demonstrate that GOES-10 provides qualitative information about regions where the semidiurnal cycle is dominant.

[29] The RMSE map between the 12-h fit and GOES-10 LWP (Figure 8a) indicates that a near-coastal area is better represented by the 12-h regression ($RMSE < 6$ g m^{-2}), whereas for its 24-h counterpart, the best agreement is found near 77°W-82°W (Figure 8b). It is interesting to observe the lack of overlap between the 12 and 24-h fits in terms of the regions having the smallest *RMSE*. The lowest *RMSE* area for the 12-h fit is fairly consistent with the region having the largest amplitude of the second harmonic (12 h) in the LWP cycle observed by *O'Dell et al.* [2008], a result that provides further evidence of the physical consistency of GOES-10 LWP retrievals with independent measures of cloud microphysics.

[30] Figure 9 shows the local time of occurrence of the minimum mean LWP, τ, and r_e, determined by independently fitting each variable with a cosine function as in equation (3). Because we cannot compute mean daily values for τ and r_e, they are calculated during the regression

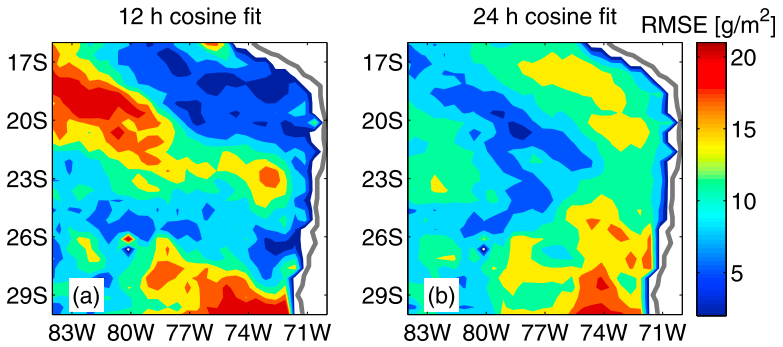

Figure 8. RMSE maps between GOES daytime cycle and (a) the 12-h regression and (b) 24-h regressions.

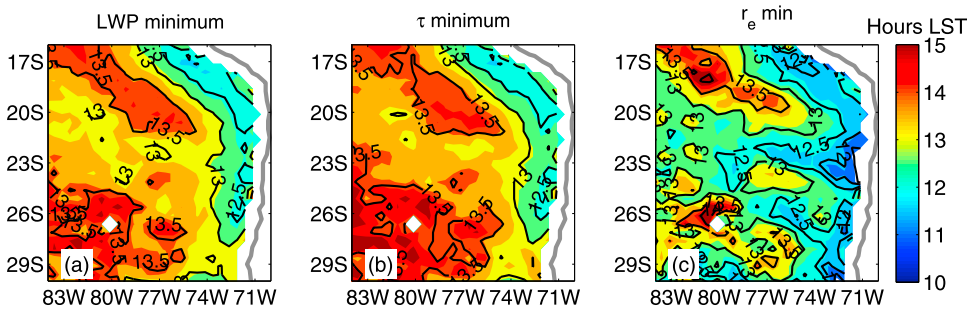

Figure 9. Time occurrence of the minimum in (a) LWP, (b) τ, and (c) r_e. Results are based on the 12 h and 24 h cosine regressions (colors and contours respectively).

process. It is important to emphasize that the purpose of fitting a cosine function is to estimate the local time occurrence of the minimum, but no inferences are made about the amplitude. The local times for the minimum LWP, τ, and r_e are calculated from the 24 and 12-h cosines (colors and contours in Figure 9). LWP (Figure 9a) and τ (Figure 9b) are in phase, reflecting the high variance of LWP explained by τ. In addition, noticeable zonal changes are manifested between near-coastal regions, with a minimum near 12:30 LST, and offshore regions, where the minimum occurs at 14 LST (for the 24-h cosine), a result consistent with Figure 7. In contrast, the r_e minima are out of phase relative to their LWP and τ counterparts. The r_e-minimum spatial pattern is relatively homogeneous, without a clear zonal trend, and typically occurs between 12:30 and 13:30 LST for the 12-h fit (Figure 9c). This further supports the idea of a different dynamical modulation in r_e and *LWP* (τ).

4.2. Daytime Evolution of τ, r_e, and N_d

[31] The regional mean daytime evolution in CF, τ, and r_e is depicted in Figure 10. The CF maps reveal the expected evolution in cloud cover, with maximum values in the morning and minima at 13:15 LST (Figure 10a). An area located at the diagonal of the 17°S-23°S, 72°W-82°W quadrant, has a CF peak from 7:15 to 13:15 LST, whereas near-coastal and far-offshore regions have larger CF variability,

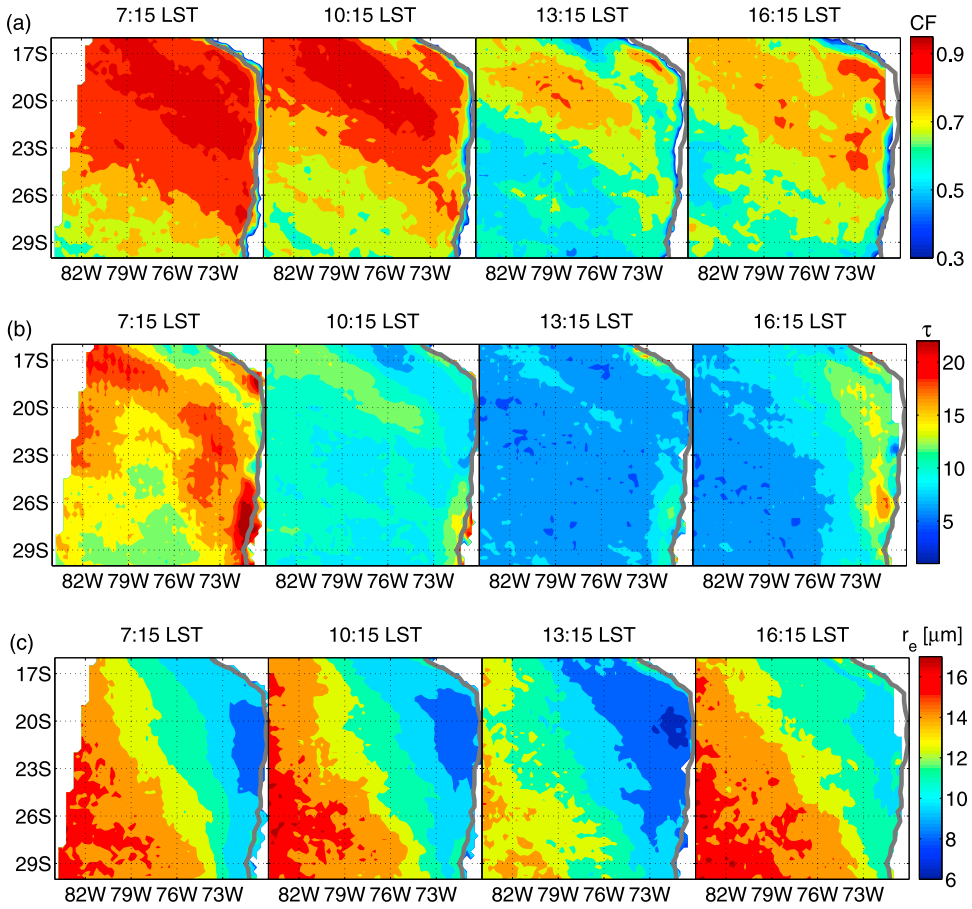

Figure 10. Daytime evolution in GOES (a) CF, (b) τ and (c) r_e.

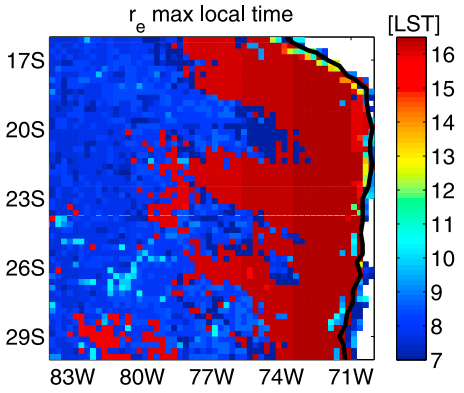

Figure 11. Solar local time occurrence of the maximum r_e.

encompassing values between 0.4 and 0.9. The dynamical factors that explain the changes in CF along the coast might be related to an enhanced afternoon above-cloud entrainment of dry and warm air from the continent [*Garreaud and Muñoz*, 2004]. Because GOES-10 can resolve the 24-h cycle in cloud cover, the investigation of the cloud fraction cycle and its link with the boundary layer evolution will be the topic of future work.

[32] Large values of τ occur at 7:15 LST, with maximum magnitudes around 20 and a peak along the coast, near 26°–30°S (Figure 10b). Three hours later, τ decreases to values between 8 and 15, maintaining a relative distribution similar to that at 7:15 LST. At 13:15 LST, τ decreases to near minimum with values smaller than 8, whereas three hours later, the τ recovery is considerable with the largest increase along the coast ($10 < \tau < 20$).

[33] In terms of r_e (Figure 10c), no significant changes are observed during the first 3 h (mean differences of 0.23 μm), with values fluctuating between 9.5 μm near the coast and 16 μm well offshore. At 13:15 LST, an overall r_e decrease over the domain is apparent, with minima at 7 μm over the Arica Bight (20°S, 71°W) and at 12.5 μm to the west. Later during the day, r_e significantly increases, with a striking daytime maximum for coastal clouds at 16:15 LST, reaching magnitudes nearly 1.5 μm larger than its 7:15 LST morning counterpart. Moreover, the times of occurrence for the maximum r_e differ between near coastal and offshore clouds, with the former attaining a r_e maximum near 16:15 UTC (as anticipated in Figure 10) and the latter during the morning at 7:45 LST (Figure 11). The question is whether the largest coastal daytime r_e at 16:15 LST can be physically explained by the atmospheric circulation/composition, or it is the consequence of retrieval artifacts attributed to the high SZA (60°-70°). Although retrieval artifacts are certainly possible, the high correlations and unbiased GOES-10 LWP relative to the TMI LWP at 16:15 (Figure 6c) suggest that retrieval artifacts such as those associated with 3D radiative effects, could be relatively well constrained in our observations.

[34] The spatial pattern of N_d in Figure 12 is fairly consistent with r_e; nevertheless, the magnitude and evolution of N_d is controlled by the competing effect of τ and r_e in equation (2). Although r_e is not at its smallest at 7:15 LST, N_d is at a maximum due to a considerably large τ. The reduction of N_d at 10:15 LST is in agreement with cloud thinning, whereas at 13:15 LST the r_e decrease counteracts the cloud thinning, producing a recovery in N_d. The largest daytime r_e along the coast, at 16:15 LST, yields the smallest N_d in our GOES-10 observations.

4.3. Two-Stream Albedo Susceptibility

[35] It is possible to compute a coarse estimate of the albedo susceptibility to changes in cloud microphysics. Here, we use two metrics of albedo susceptibility [*Platnick and Oreopoulos*, 2008; *Painemal and Minnis*, 2012] defined as:

$$S = \frac{dA}{dN_d}, \; S_R = \frac{dA}{d\ln N_d}. \tag{4}$$

[36] Where A is the albedo at the top of the atmosphere, and S and S_R are the absolute and relative (fractional) albedo susceptibility to changes in N_d,, respectively. These metrics relate changes in N_d, modulated by the cloud dynamics and the aerosol concentration, to actual changes in the planetary albedo. S and S_R can be approximated using the two-stream approximation as:

$$S = \frac{A_{cloud}(1 - A_{cloud})}{3N_d} \tag{5}$$

$$S_{R-2S} = \frac{A_{cloud}(1 - A_{cloud})}{3} \tag{6}$$

[37] The two-stream cloud albedo A_{cloud} is:

$$A_{cloud} = \frac{\tau(1-g)}{2 + (1-g)\tau} \tag{7}$$

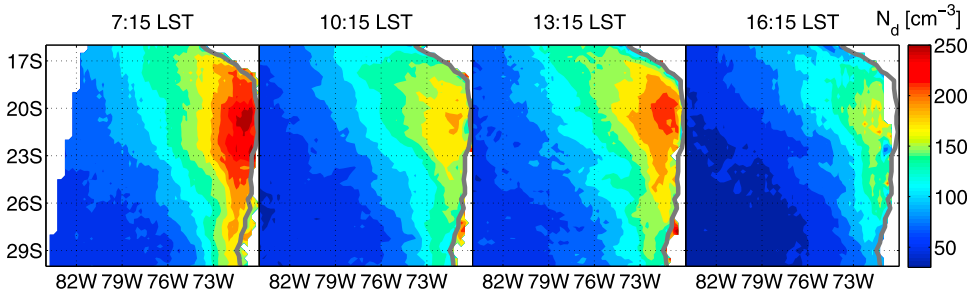

Figure 12. Daytime evolution of GOES N_d.

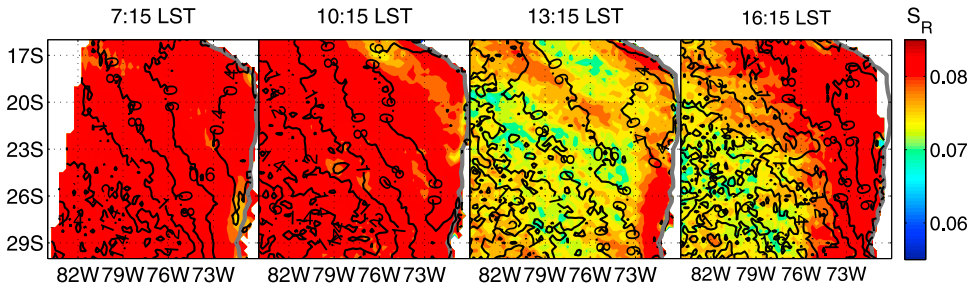

Figure 13. Daytime evolution of two-stream GOES relative susceptibility (S_R, colors) and absolute susceptibility in mm^{-3} (contours).

[38] The asymmetry parameter g is assumed constant at 0.85. Despite the fact that equations (5) and (6) are approximations of the cloud radiative response and they do not account for the atmospheric composition (that is, they are not top-of-the-atmosphere estimates), they do provide qualitative information of the actual albedo susceptibility [*Painemal and Minnis*, 2012].

[39] The S and S_R distributions computed using equations (5) and (6) are depicted in Figure 13 (contours and colors respectively). In terms of S_R, the morning values are close to the theoretical maximum (0.083), associated with τ larger than the value that maximizes S_R in equation (6) ($\tau = 13.3$). S_R decreases at 13:15 LST, whereas a recovery at 16:15 is mainly led by the coastal clouds. The values of S show the typical spatial pattern described in *Painemal and Minnis* [2012] and is anti-correlated with N_d (Figure 12). Since the largest changes in N_d are found along the coast, S tends to be more variable in this region, whereas changes in S are negligible throughout the day for offshore clouds. It is remarkable that the values of both S and S_R are smallest at 13:15 LST over the Arica Bight, This result indicates that the albedo of the cloud deck is least sensitive at that time to changes in cloud microphysics.

5. Discussion

[40] Uncertainties in GOES-10 retrievals can be determined by assuming errors in the measured radiances and in the atmospheric composition. For instance, *Dong et al.* [2008] reported mean uncertainties of 15% (r_e) and 8% (τ) for retrievals produced with the GOES/CERES algorithm. In agreement with this assessment, the MODIS team uncertainty product indicates mean values of 16% and 12% in r_e and τ, respectively.

[41] Other errors, difficult to quantify operationally, are those associated with 3D radiative effects and their dependence on the satellite/solar viewing geometry [e.g., *Kato et al.*, 2006]. Interestingly, the good match between GOES-10 and microwave LWPs for high solar zenith angles (SZA > 60°, biases smaller than 10.2%), which are associated with greater 3D radiative effects, suggest that errors attributed to cloud spatial heterogeneities are well constrained over the region. Additionally, the good agreement between the GOES-10 and MODIS Atmosphere Team retrievals indicate that GOES-10 infrared original pixel resolution (~4 km) is not severely affected (<10%) by clear sky sub-pixel variability relative to the 1 km resolution MODIS product. This relative insensitivity to 3D radiative effects and sub-pixel variability is consistent with the region's high horizontal homogeneity [*Di Girolamo et al.*, 2010] and persistent cloud cover [*Klein and Hartmann*, 1993].

[42] The C-130 aircraft observations used here were collected over a broad oceanic domain that possesses a high spatial variability in cloud properties (PZ11). Thus, these in situ retrievals were not suitable to evaluate the GOES-10 daytime cycle. Nevertheless, *Zheng et al.* [2011] found that the stratocumulus LWP derived from independent in situ measurements during morning hours over Point Alpha (20°S, 72°W) was, on average, 3.4 ± 19.9 g m^{-2} less than the GOES-10 retrievals with $r^2 = 0.84$. These results are consistent with the comparisons of SSM/I and GOES-10 retrievals (Table 3). This suggests that the diurnal signal from GOES-10 would be consistent with that derived from more systematic in situ measurements.

[43] Similar to the τ results, the GOES-10 r_e cycle is consistent with other investigations over the west coast of California [*Minnis et al.*, 1992; *Greenwald and Christopher*, 1999]. In contrast, our findings show a broad disagreement with *Matsui et al.* [2006] and their global daytime r_e cycle derived from LWP and τ collected by TRMM over maritime warm clouds. *Matsui et al.* [2006] observed r_e magnitudes between 14 and 25 μm with a modest daytime cycle in LWP, indicating that their results are more applicable to convective clouds, where 3D radiative transfer effects might be more severe.

[44] *Oku et al.* [2010] also report a maximum in coastal r_e values during the afternoon but over continental clouds in eastern Asia (not limited to stratocumulus), using a different geostationary satellite imager. Similarly, *Han et al.* [1994] support the idea of a maximum r_e occurrence during the afternoon, although in their study this maximum was not necessarily confined to the coastal regions. If not an algorithm artifact, what are the physical processes that drive this afternoon maximum? The explanation could be related to the same processes that produce the fastest coastal τ recovery at 16:15 UTC, over the same region. Although the τ recovery must be partially associated with higher solar zenith angle and therefore reduction of solar heating, additional forcing should account for the distinctive westward contrast in τ. Modeling evidence indicates that a vertical velocity wave, driven by heating of the Andes, produces dominant updrafts along the coast at 16:00 local time [*Rahn and Garreaud*, 2010]. These updrafts should contribute to increased liquid water path and optical thickness, as well as enhanced droplet sizes, arguably through condensational growth. In addition, the relative lack of a pattern for the minimum r_e occurrence

(near 12:30 LST) throughout the domain suggests that this is mainly controlled by droplet evaporation due to solar heating. A second element to take into account is the cloud top entrainment. In this regard, cloud observations collected during VOCALS-REx (PZ11) indicate that the cloud top mixing is inhomogeneous, which would produce total evaporation of some drops, but r_e would remain relatively constant. In contrast, it is likely that the entrainment-induced evaporation might significantly modify LWP (τ), and plausibly reconciles different LWP and r_e phases.

[45] Attributing physical mechanisms to the N_d daytime evolution is difficult, because the N_d parameterization can be sensitive to assumptions about the cloud vertical structure and adiabaticity. Nevertheless, dramatic changes in LWP allow one to hypothesize that changes in N_d are mainly driven by the local circulation and solar heating.

[46] It is important to emphasize that our analysis is limited to spring, the season with the most extensive development of the southeast Pacific stratocumulus cloud deck, and therefore, the results might differ from those obtained in other seasons. During autumn/winter, the cloud deck is more influenced by midlatitude synoptic intrusions, producing large changes in temperature advection and regional scale subsidence [*Painemal et al.*, 2010]. In addition, the reduced shortwave absorption, and the decrease in liquid water attributed to synoptic activity, produces diurnal amplitudes in cloud fraction and LWP that are smaller relative to those during summer/spring [*Painemal et al.*, 2010].

6. Concluding Remarks

[47] Cloud property retrievals based on GOES-10 imager visible and infrared radiances were used to investigate the daytime cycle in cloud microphysics within the southeast Pacific stratocumulus cloud regime during October–November 2008. The retrieval accuracies were assessed with satellite microwave LWP, and MODIS retrievals produced with two different algorithms. The good agreement between GOES-10 retrievals and independent data sets lends confidence in the ability of using GOES-10 retrievals to represent the daytime cycle. Despite the good general GOES-10 performance, GOES-10 overestimates r_e relative to the aircraft in situ observed r_e by about 2.3 μm, comparable to a MODIS bias of 2 μm over the same region (PZ11). The explanation for this positive bias remains elusive.

[48] Regarding MODIS Terra/Aqua differences, a new CERES edition 4 product that accounts for differences between the Terra and Aqua calibrations [*Minnis et al.*, 2010], will allow determination of the extent to which the MODIS-Terra biases are likely the consequence of un-calibrated radiances.

[49] Analysis of the GOES-10 LWP estimate reveals that GOES-10 provides reliable information on the diurnal and semidiurnal cycles of the microphysical properties of marine stratocumulus clouds. Based on the daytime evolution of τ, we determined that τ and LWP are in phase with a similar cycle, a result consistent with the high LWP variance explained by τ. The local time for the minimum τ (14–15 UTC) in offshore clouds is in agreement with *Minnis et al.* [1992] and *Greenwald and Christopher* [1999], although distinctive τ spatial differences are present, with minimum τ occurring near noon over coastal areas, suggesting a daytime cycle modulated by semidiurnal scale processes, similar to those controlling LWP.

[50] An afternoon τ recovery lead by near coastal clouds, and concomitant with maxima r_e, indicate that coastal processes may play an important role in the diurnal microphysical evolution. This pattern is consistent with a positive vertical velocity wave originated by the Andes heating during the afternoon [*Rahn and Garreaud*, 2010].

[51] The overall changes in cloud microphysics have a significant impact on the cloud albedo, especially around 13:15 LST when a 11% albedo decrease relative to the mean state is associated with the largest decrease in τ (20%). Future estimates of albedo susceptibility should take into account these diurnal variations; therefore, caution should be taken when calculating cloud radiative effects from only one daily satellite overpass.

[52] While this work presents the first systematic investigation of the daytime cycle over this region, the results require further validation with in situ and independent satellite observations. The underlying physics behind the diurnal cycle will require careful modeling efforts that take into account the conspicuous differences between coastal and offshore meteorology.

[53] **Acknowledgments.** D. Painemal was supported by the NASA Postdoctoral Program at the NASA Langley Research Center, administered by Oak Ridge Associated Universities (ORAU). P. Minnis and J. K. Ayers were supported by the NASA Modeling, Analysis, and Prediction and CERES Programs, and by the U.S. Department of Energy's Atmospheric Science Program Atmospheric System Research interagency Agreement, DE-SC0000991/003. L. O'Neill was supported by NASA grant NNX11AF31G for funding of NASA's Ocean Vector Winds Science Team activities and an Institutional Postdoctoral Fellowship through Oregon State University. The suggestions made by three anonymous reviewers are also greatly acknowledged.

References

Ackerman, A., M. Kirkpatrick, D. Stevens, and O. Toon (2004), The impact of humidity above stratiform clouds on indirect aerosol climate forcing, *Nature*, *432*, 1014–1017, doi:10.1038/nature03174.

Bennartz, R. (2007), Global assessment of marine boundary layer cloud droplet number concentration from satellite, *J. Geophys. Res.*, *112*, D02201, doi:10.1029/2006JD007547.

Bony, S., and J.-L. Dufresne (2005), Marine boundary layer clouds at the heart of tropical cloud feedback uncertainties in climate models, *Geophys. Res. Lett.*, *32*, L20806, doi:10.1029/2005GL023851.

Borg, L. A., and R. Bennartz (2007), Vertical structure of stratiform marine boundary layer clouds and its impact on cloud albedo, *Geophys. Res. Lett.*, *34*, L05807, doi:10.1029/2006GL028713.

Cahalan, R. F., W. Ridgway, W. J. Wiscombe, T. L. Bell, and J. B. Snider (1994), The albedo of fractal stratocumulus clouds, *J. Atmos. Sci.*, *51*, 2434–2455, doi:10.1175/1520-0469(1994)051<2434:TAOFSC>2.0.CO;2.

Di Girolamo, L., L. Liang, and S. Platnick (2010), A global view of one-dimensional solar radiative transfer through oceanic water clouds, *Geophys. Res. Lett.*, *37*, L18809, doi:10.1029/2010GL044094.

Dong, X., P. Minnis, B. Xi, S. Sun-Mack, and Y. Chen (2008), Comparison of CERES-MODIS stratus cloud properties with ground-based measurements at the DOE ARM Southern Great Plains site, *J. Geophys. Res.*, *113*, D03204, doi:10.1029/2007JD008438.

Garreaud, R. D., and R. Muñoz (2004), The diurnal cycle of circulation and cloudiness over the subtropical southeast Pacific: A modeling study, *J. Clim.*, *17*, 1699–1710, doi:10.1175/1520-0442(2004)017<1699:TDCICA>2.0.CO;2.

Greenwald, T. J., and S. A. Christopher (1999), Daytime variation of marine stratocumulus microphysical properties as observed from geostationary satellite, *Geophys. Res. Lett.*, *26*(12), 1723–1726, doi:10.1029/1999GL900346.

Han, Q. Y., W. B. Rossow, and A. A. Lacis (1994), Near-global survey of effective droplet radii in liquid water clouds using ISCCP data, *J. Clim.*, *7*, 465–497, doi:10.1175/1520-0442(1994)007<0465:NGSOED>2.0.CO;2.

Hannay, C., D. L. Williamson, J. J. Hack, J. T. Kiehl, J. G. Olson, S. A. Klein, C. S. Bretherton, and M. Köhler (2009), Evaluation of

forecasted southeast Pacific stratocumulus in the NCAR, GFDL, and ECMWF models, *J. Clim.*, *22*, 2871–2889, doi:10.1175/2008JCLI2479.1.

Hilburn, K. A., and F. J. Wentz (2008), Intercalibrated passive microwave rain products from the Unified Microwave Ocean Retrieval Algorithm (UMORA), *J. Appl. Meteorol. Climatol.*, *47*, 778–794, doi:10.1175/2007JAMC1635.1.

Horváth, Á., and C. Gentemann (2007), Cloud-fraction-dependent bias in satellite liquid water path retrievals of shallow, non-precipitating marine clouds, *Geophys. Res. Lett.*, *34*, L22806, doi:10.1029/2007GL030625.

Kato, S., L. M. Hinkelman, and A. Cheng (2006), Estimate of satellite-derived cloud optical thickness and effective radius errors and their effect on computed domain-averaged irradiances, *J. Geophys. Res.*, *111*, D17201, doi:10.1029/2005JD006668.

Klein, S. A., and D. L. Hartmann (1993), The seasonal cycle of low stratiform clouds, *J. Clim.*, *6*, 1587–1606, doi:10.1175/1520-0442(1993)006<1587:TSCOLS>2.0.CO;2.

Matsui, T., H. Masunaga, S. M. Kreidenweis, R. A. Pielke Sr., W.-K. Tao, M. Chin, and Y. J. Kaufman (2006), Satellite-based assessment of marine low cloud variability associated with aerosol, atmospheric stability, and the diurnal cycle, *J. Geophys. Res.*, *111*, D17204, doi:10.1029/2005JD006097.

Minnis, P. (1989), Viewing zenith angle dependence of cloudiness determined from coincident GOES East and GOES West data, *J. Geophys. Res.*, *94*(D2), 2303–2320, doi:10.1029/JD094iD02p02303.

Minnis, P., and E. F. Harrison (1984), Diurnal variability of regional cloud and clear-sky radiative parameters derived from GOES data, Part II: November 1978 cloud distributions, *J. Clim. Appl. Meteorol.*, *23*, 1012–1031, doi:10.1175/1520-0450(1984)023<1012:DVORCA>2.0.CO;2.

Minnis, P., P. W. Heck, D. F. Young, C. W. Fairall, and J. B. Snider (1992), Stratocumulus cloud properties derived from simultaneous satellite and island-based instrumentation during FIRE, *J. Appl. Meteorol.*, *31*, 317–339, doi:10.1175/1520-0450(1992)031<0317:SCPDFS>2.0.CO;2.

Minnis, P., L. Nguyen, D. R. Doelling, D. F. Young, W. F. Miller, and D. P. Kratz (2002), Rapid calibration of operational and research meteorological satellite imagers, Part I: Evaluation of research satellite visible channels as references, *J. Atmos. Oceanic Technol.*, *19*, 1233–1249, doi:10.1175/1520-0426(2002)019<1233:RCOOAR>2.0.CO;2.

Minnis, P., et al. (2008a), Cloud detection in non-polar regions for CERES using TRMM VIRS and Terra and Aqua MODIS data, *IEEE Trans. Geosci. Remote Sens.*, *46*, 3857–3884, doi:10.1109/TGRS.2008.2001351.

Minnis, P., et al. (2008b), Near-real time cloud retrievals from operational and research meteorological satellites, *Proc. SPIE Int. Soc. Opt. Eng.*, *7107*, 710703, doi:10.1117/12.800344.

Minnis, P., D. R. Doelling, L. Nguyen, W. F. Miller, and V. Chakrapani (2008c), Assessment of the visible channel calibrations of the VIRS on TRMM and MODIS on Aqua and Terra, *J. Atmos. Oceanic Technol.*, *25*, 385–400, doi:10.1175/2007JTECHA1021.1.

Minnis, P., et al. (2010), CERES Edition 3 cloud retrievals, paper presented at 13th Conference on Atmospheric Radiation, AMS, Portland, Oreg.

Minnis, P., et al. (2011), CERES Edition-2 cloud property retrievals using TRMM VIRS and Terra and Aqua MODIS data. Part I: Algorithms, *IEEE Trans. Geosci. Remote Sens.*, *49*(11), 4374–4400, doi:10.1109/TGRS.2011.2144601.

Minnis, P., et al. (2012), CERES Edition-2 cloud property retrievals using TRMM VIRS and Terra and Aqua MODIS data, Part II: Examples of average results and comparisons with other data, *IEEE Trans. Geosci. Remote Sens.*, doi:10.1109/TGRS.2011.2144602, in press.

O'Dell, C. W., F. J. Wentz, and R. Bennartz (2008), Cloud liquid water path from satellite-based passive microwave observations: A new climatology over the global oceans, *J. Clim.*, *21*, 1721–1739, doi:10.1175/2007JCLI1958.1.

Oku, Y., M. Kajino, and H. Ishikawa (2010), Estimation of the cloud effective particle radius using MTSAT-1R data, *Int. J. Remote Sens.*, *31*(20), 5439–5447, doi:10.1080/01431160903369634.

O'Neill, L. W., S. Wang, and Q. Jiang (2011), Satellite climatology of cloud liquid water path over the Southeast Pacific between 2002 and 2009, *Atmos. Chem. Phys. Discuss.*, *11*, 31,159–31,206, doi:10.5194/acpd-11-31159-2011.

Painemal, D., and P. Minnis (2012), On the dependence of albedo on cloud microphysics over marine stratocumulus clouds regimes determined from CERES data, *J. Geophys. Res.*, *117*, D06203, doi:10.1029/2011JD017120.

Painemal, D., and P. Zuidema (2010), Microphysical variability in southeast Pacific Stratocumulus clouds: Synoptic conditions and radiative response, *Atmos. Chem. Phys.*, *10*, 6255–6269, doi:10.5194/acp-10-6255-2010.

Painemal, D., and P. Zuidema (2011), Assessment of MODIS cloud effective radius and optical thickness retrievals over the southeast Pacific with VOCALS-Rex in situ measurements, *J. Geophys. Res.*, *116*, D24206, doi:10.1029/2011JD016155.

Painemal, D., R. Garreaud, J. Rutllant, and P. Zuidema (2010), Southeast Pacific stratocumulus: High-frequency variability and mesoscale structures over San Félix Island, *J. Appl. Meteorol. Climatol.*, *49*, 463–477, doi:10.1175/2009JAMC2230.1.

Platnick, S., and L. Oreopoulos (2008), Radiative susceptibility of cloudy atmospheres to droplet number perturbations: 1. Theoretical analysis and examples from MODIS, *J. Geophys. Res.*, *113*, D14S20, doi:10.1029/2007JD009654.

Platnick, S., M. King, S. Ackerman, W. Menzel, B. Baum, J. Riedi, and R. Frey (2003), The MODIS cloud products: Algorithms and examples from Terra, *IEEE Trans. Geosci. Remote Sens.*, *41*, 459–473, doi:10.1109/TGRS.2002.808301.

Rahn, D. A., and R. Garreaud (2010), Marine boundary layer over the subtropical southeast Pacific during VOCALS-REx–Part 1: Mean structure and diurnal cycle, *Atmos. Chem. Phys.*, *10*, 4491–4506, doi:10.5194/acp-10-4491-2010.

Rozendaal, M., C. Leovy, and S. Klein (1995), An observational study of diurnal variations of marine stratiform cloud, *J. Clim.*, *8*, 1795–1809, doi:10.1175/1520-0442(1995)008<1795:AOSODV>2.0.CO;2.

Sandu, I., J.-L. Brenguier, O. Geoffroy, O. Thouron, and V. Masson (2008), Aerosol impacts on the diurnal cycle of marine stratocumulus, *J. Atmos. Sci.*, *65*, 2705–2718, doi:10.1175/2008JAS2451.1.

Seethala, C., and Á. Horváth (2010), Global assessment of AMSR-E and MODIS cloud liquid water path retrievals in warm oceanic clouds, *J. Geophys. Res.*, *115*, D13202, doi:10.1029/2009JD012662.

Wang, S., L. W. O'Neill, Q. Jiang, S. P. de Szoeke, X. Hong, H. Jin, W. T. Thompson, and X. Zheng (2011), A regional real-time forecast of marine boundary layers during VOCALS-REx, *Atmos. Chem. Phys.*, *11*, 421–437, doi:10.5194/acp-11-421-2011.

Wentz, F. (1997), A well-calibrated ocean algorithm for Special Sensor Microwave/Imager, *J. Geophys. Res.*, *102*, 8703–8718, doi:10.1029/96JC01751.

Wentz, F., and T. Meissner (2000), AMSR ocean algorithm, *Algorithm Theor. Basis Doc. 121599A-1*, Remote Sens. Syst., Santa Rosa, Calif.

Wood, R., C. S. Bretherton, and D. L. Hartmann (2002), Diurnal cycle of liquid water path over the subtropical and tropical oceans, *Geophys. Res. Lett.*, *29*(23), 2092, doi:10.1029/2002GL015371.

Wood, R., M. Kohler, R. Bennartz, and C. O'Dell (2009), The diurnal cycle of surface divergence over the global oceans, *Q. J. R. Meteorol. Soc.*, *135*, 1484–1493, doi:10.1002/qj.451.

Wood, R., et al. (2011), The VAMOS Ocean-Cloud-Atmosphere-Land Study Regional Experiment (VOCALS-Rex): Goals, platforms, and field operations, *Atmos. Chem. Phys.*, *11*, 627–654, doi:10.5194/acp-11-627-2011.

Young, D. F., P. Minnis, G. G. Gibson, D. R. Doelling, and T. Wong (1998), Temporal interpolation methods for the clouds and Earth's Radiant Energy System (CERES) Experiment, *J. Appl. Meteorol.*, *37*, 572–590, doi:10.1175/1520-0450(1998)037<0572:TIMFTC>2.0.CO;2.

Zhang, Z., and S. Platnick (2011), An assessment of differences between cloud effective particle radius retrievals for marine water clouds from three MODIS spectral bands, *J. Geophys. Res.*, *116*, D20215, doi:10.1029/2011JD016216.

Zheng, X., et al. (2011), Observations of the boundary layer, cloud, and aerosol variability in the southeast Pacific near-coastal marine stratocumulus during VOCALS-REx, *Atmos. Chem. Phys.*, *11*, 9943–9959, doi:10.5194/acp-11-9943-2011.

Zuidema, P., and D. L. Hartmann (1995), Satellite determination of stratus cloud microphysical properties, *J. Clim.*, *8*, 1638–1656.

Zuidema, P., D. Painemal, S. de Szoeke, and C. Fairall (2009), Stratocumulus cloud top estimates and their climatic implications, *J. Clim.*, *22*, 4652–4666, doi:10.1175/2009JCLI2708.1.